

Mechanism and microkinetics of methanol synthesis *via* CO₂ hydrogenation on indium oxide

M.S. Frei^a, M. Capdevila-Cortada^b, R. García-Muelas^b, C. Mondelli^a, N. López^{b,*}, J.A. Stewart^c, D. Curulla Ferré^c, J. Pérez-Ramírez^{a,*}

^aInstitute for Chemical and Bioengineering, Department of Chemistry and Applied Biosciences, ETH Zurich, Vladimir-Prelog-Weg 1, 8093 Zürich, Switzerland

^bInstitute of Chemical Research of Catalonia, ICIQ, The Barcelona Institute of Science and Technology, Av. Països Catalans 16, 43007 Tarragona, Spain

^cTotal Research & Technology Feluy, Zone Industrielle Feluy C, 7181 Seneffe, Belgium

A B S T R A C T

Indium oxide has emerged as a highly effective catalyst for methanol synthesis by direct CO₂ hydrogenation. Aiming at gathering a deeper fundamental understanding, mechanistic and (micro)kinetic aspects of this catalytic system were investigated. Steady-state evaluation at 5 MPa and variable temperature indicated a lower apparent activation energy for CO₂ hydrogenation than for the reverse water-gas shift reaction (103 versus 117 kJ mol⁻¹), which is in line with the high methanol selectivity observed. Upon changing the partial pressure of reactants and products, apparent reaction orders of -0.1, 0.5, -0.2, and -0.9 were determined for CO₂, H₂, methanol, and water, respectively, which highlight a strong inhibition by the latter. Co-feeding of H₂O led to catalyst deactivation by sintering for partial pressures exceeding 0.125 MPa, while addition of the byproduct CO to the gas stream could be favorable at a total pressure below 4 MPa but was detrimental at higher pressures. Density Functional Theory simulations conducted on In₂O₃(1 1 1), which was experimentally and theoretically shown to be the most exposed surface termination, indicated that oxygen vacancies surrounded by three indium atoms enable the activation of CO₂ and split hydrogen heterolytically, stabilizing the polarized species formed. The most energetically favored path to methanol comprises three consecutive additions of hydrides and protons and features CH₂OOH and CH₂(OH)₂ as intermediates. Microkinetic modeling based on the DFT results provided values for temperature and concentration-dependent parameters, which are in good agreement with the empirically obtained data. These results are expected to drive further optimization of In₂O₃-based materials and serve as a solid basis for reactor and process design, thus fostering advances towards a potential large-scale methanol synthesis from CO₂.

1. Introduction

Aiming at mitigating global warming, the utilization of CO₂ captured either from the atmosphere or from localized emission points as a feedstock for the production of fuels and chemicals has taken center stage in catalysis research in the last decade [1,2]. Among the routes investigated for the conversion of this rather inert molecule, hydrogenation to methanol has attracted particular attention owing to the extreme relevance of this alcohol for the chemical industry and the energy sector [3]. At present, the industrial synthesis of methanol is carried out from syngas, which is predominantly derived from steam reforming of fossil fuels, in the presence of small amounts (3 vol%) of CO₂ over Cu-ZnO-Al₂O₃

catalysts [4]. When CO₂ is the only carbon-containing source (CO₂ + 3H₂ ⇌ CH₃OH + H₂O), these catalysts exhibit limited activity, selectivity, and stability. Particularly, the production of methanol is suppressed by the competitive reverse water-gas shift (RWGS) reaction (CO₂ + H₂ ⇌ CO + H₂O) [5]. Therefore, alternative catalytic systems are sought after to enable the development of a CO₂-to-methanol technology [6]. Among the materials investigated, a few Cu-based solids exhibited high methanol selectivity but their long-term stability was not demonstrated [7,8]. In contrast, indium oxide, In₂O₃, emerged as a catalyst combining multiple desirable features [9]. In addition to being highly selective to methanol, it can be easily supported on zirconia, leading to higher methanol formation rates and outstanding durability, and prepared in an equivalently performing technical form [10]. Its potential for a prospective industrial implementation has motivated further practically-oriented studies. Indeed, it has been reported that In₂O₃ can be used in bifunctional catalytic systems

* Corresponding authors.

E-mail addresses: nlopez@iciq.es (N. López), jpr@chem.ethz.ch (J. Pérez-Ramírez).

[11,12] to produce olefins from CO₂ and that its activity in methanol synthesis can be enhanced through the addition of a noble metal such as Pd, which is claimed to facilitate hydrogen splitting [13,14]. Furthermore, it sparked the idea of combining another reducible oxide, ZnO, with zirconia, attaining a remarkable catalyst [15]. In contrast, fundamental aspects of CO₂ hydrogenation over In₂O₃, such as the reaction mechanism and kinetics, remain insufficiently understood, thus hindering the optimization of this catalytic process. Under the conditions commonly applied (573 K, 5 MPa, molar H₂:CO₂ = 4), the thermodynamic equilibrium highly favors the endothermic RWGS reaction over the exothermic hydrogenation to methanol [16]. Hence, the reaction must be carried out under kinetic control to attain a high selectivity to methanol. Nevertheless, basic kinetic information such as the temperature dependence of the transformation and the effect of the partial pressure of reactants and products has not been reported. Characterization through thermal and spectroscopic techniques and CO co-feeding experiments over bulk and ZrO₂-supported In₂O₃ strongly suggested surface oxygen vacancies as the sites where CO₂ and H₂ are activated [10]. This is in line with Density Functional Theory (DFT) studies by Ge et al. [17,18] and Yu et al. [19], which predicted a superior performance for an oxygen defective In₂O₃(1 1 0) surface compared to the stoichiometric termination and supported the high methanol selectivity on the basis of greater barriers for the RWGS reaction over the same vacancy-containing surface. Still, the orientation of the surface employed in these studies is not that being associated with the lowest energy (i.e., the most exposed). Indeed, the (1 1 1) facet is the thermodynamically most stable termination of In₂O₃ [20]. In addition, since the electronic structure of this material is rather subtle, the structures of the adsorbates need to be evaluated with some further restrictions to ensure that forbidden energy levels are not artificially populated.

Herein, we investigate the kinetic fingerprints of the CO₂ hydrogenation over bulk In₂O₃ by means of a detailed study covering a wide range of temperature (473–673 K), pressure (1–5 MPa), and reactant (CO₂, H₂) and product (CO, methanol, H₂O) concentrations. These data are correlated with extensive DFT simulations describing the energetics of the reaction over the In₂O₃(1 1 1) surface and a microkinetic model. Based on the information obtained at the experimental and theoretical levels, key conclusions are put forward on the operation of this oxide in CO₂ hydrogenation, which set the ground for its more efficient utilization in this relevant reaction.

2. Experimental

2.1. Catalyst preparation

In(OH)₃ was obtained by precipitation adding 150 cm³ of a solution of aqueous NH₄OH (50 cm³, 25 wt%, Sigma-Aldrich) in ethanol (150 cm³) to a solution of In(NO₃)₃·xH₂O (30.1 g, Sigma-Aldrich, 99.99%) in deionized water (120 cm³) and ethanol (350 cm³, Merck, 99.8%) to reach a pH value of 9.2. The resulting slurry was aged for 20 min at 353 K and then separated by high-pressure filtration and washed twice with deionized water (1000 cm³ each time) followed by drying in a vacuum oven (2 kPa, 323 K, 12 h). The so-obtained hydroxide was calcined for 3 h at 573 K (2 K min⁻¹) in static air to yield nanocrystalline In₂O₃.

2.2. Catalyst characterization

Powder X-ray diffraction (XRD) was performed using a PANalytical X'Pert PRO-MPD diffractometer with Ni-filtered Cu K α radiation (λ = 0.1541 nm), acquiring data in the 5–70°

2 θ range with a step size of 0.05° and a counting time of 12 s per step. The average particle size of In₂O₃ was estimated applying the Scherrer equation. Nitrogen sorption at 77 K was carried out using a Quantacrome Quadrasorb analyzer. Prior to the measurement, the sample was degassed at 573 K under vacuum for 3 h. He pycnometry was conducted at ambient temperature using a Micromeritics AccuPyc II 1340 instrument after pretreatment of the sample in vacuum at 323 K for 12 h. The skeletal density was determined by averaging 200 measurement cycles after equilibration of the system during 30 cycles. High resolution transmission electron microscopy (HRTEM) was performed using a FEI Talos (200 kV) instrument. Samples were prepared by directly depositing the powders on a lacey carbon film supported onto a copper grid. Temperature-programmed desorption of carbon dioxide, water, and methanol (CO₂-, H₂O-, MeOH-TPD) and reduction with hydrogen (H₂-TPR) were conducted using a Micromeritics AutoChem II 2920 analyzer. The specific conditions applied during each measurement are detailed in Table S1 in the Supplementary Material. UV-vis spectroscopy was carried out using an Ocean Optics Maya2000-Pro spectrometer equipped with a deuterium light source. Spectra were collected in the 200–600 nm range, with an integration time of 100 ms and averaging 50 scans. Raman spectroscopy was performed using a WITec CRM200 confocal Raman spectroscopy system comprising a source with an excitation wavelength of 532 nm, a 100 \times objective lens with a numerical aperture of 0.9, and a grating spectrometer (2400 lines mm⁻¹). Spectra were obtained by averaging 200 scans with an individual acquisition time of 1.5 s.

2.3. Kinetic evaluation

Kinetic investigations were performed in a high-pressure continuous-flow fixed-bed reactor with an inner diameter of 2.2 mm housed in an electrically-heated aluminum brass furnace. The experimental setup is described in detail in Fig. S1. The reactor was loaded with 25 or 50 mg of catalyst with a particle size of 100–125 μ m, which was held in place by a bed of quartz wool and heated from ambient temperature to 573 K (5 K min⁻¹) at 0.5 MPa under a He (PanGas, \geq 99.999%) flow of 20 cm³_{STP} min⁻¹. After 3 h at 573 K, the pressure was raised to 3.5–5.5 MPa in the same stream, which typically took 20 min. Then, the gas flow was switched to the reaction mixture (20 or 40 cm³_{STP} min⁻¹) featuring distinct concentrations of CO₂ (40 mol% CO₂ in H₂, Messer, \geq 99.997% and \geq 99.999%, respectively), H₂ (PanGas, \geq 99.999%), methanol (Sigma-Aldrich, 99.9%, anhydrous), H₂O (ABCR-Chemicals, HPLC grade), and CO (Messer, \geq 99.999%), corresponding to a gas-hourly space-velocity (GSHV) of 38,000 h⁻¹. The temperature was either kept at 573 K or varied in the range of 473–673 K. The specific experimental conditions applied in the tests are collected in Table 1. The effluent stream was analyzed by gas chromatography after 1 h on stream and then every 20 min. The catalytic data reported for each reaction condition correspond to the average of at least 7 measurements. The absence of intra- and extraparticle diffusion limitations was corroborated by the fulfillment of the Weisz-Prater and Carberry criteria and secured by a test in which a catalyst sample featuring a sieve fraction of <50 μ m instead of the typical 100–125 μ m was applied that led to identical performance.

2.4. Computational methods

DFT calculations were conducted using the Vienna *Ab initio* Simulation Package (VASP) [21,22], employing the Perdew-Burke-Ernzerhof (PBE) exchange-correlation functional [23]. The core electrons were described by projector augmented-wave pseudopotentials (PAW) [24] with a plane-wave cutoff energy of

Table 1
Conditions applied in the steady-state kinetic experiments.

Experiment	Catalyst mass [mg]	Initial gas feed ^a [cm _{STP} ³ min ⁻¹]	Step changes applied to flow ^b [cm _{STP} ³ min ⁻¹]	Final gas feed [cm _{STP} ³ min ⁻¹]	Temperature [K]	Total pressure [MPa]
Determination of activation energies (Fig. 2a)	50	CO ₂ : 8 H ₂ : 32		8 32	473–673 ^c	5
Determination of reaction order with respect to CO ₂ and H ₂ (Fig. 2b)	25	CO ₂ : 8 H ₂ : 12	–0.8 +0.8	0.8 19.2	573	5
Determination of reaction order with respect to MeOH (Fig. 2c)	50	CO ₂ : 8 H ₂ : 32 MeOH: 0	–0.1 –0.4 +0.5	7.5 30 2.5	573	5
Determination of reaction order with respect to H ₂ O (Fig. 2c)	50	CO ₂ : 8 H ₂ : 32 H ₂ O: 0	–0.08 –0.32 +0.4	7.6 30.4 2	573	5
Impact of low CO concentration on the catalyst (Fig. 4a)	25	CO ₂ : 4 H ₂ : 16 He: 4 CO: 0	–1 +1	4 16 0 4	573	3.5, 4.5, or 5.5
Assessment of deactivation by CO (Fig. 4b)	25	CO ₂ : 4 H ₂ : 16 CO: 0 He: 4	+1, 2.5, or 4 –1, 2.5, or 4	4 16 1, 2.5, or 4 ^d 3, 1.5, or 0 ^d	573	5.5
Assessment of deactivation by H ₂ O (Fig. S6)	50	CO ₂ : 8 H ₂ : 32 H ₂ O: 0	–0.5 –0.5 +1	7.5 31.5 1	573	5

^a In all experiments a constant flow of 2.5 cm_{STP}³ min⁻¹ of 20 mol% CH₄ in He was added to the effluent stream as an internal standard.

^b As many steps as needed to reach the final gas feed were applied.

^c The temperature was increased stepwise by 25 K.

^d After 3 h on stream the initial values were restored.

500 eV for the valence electrons (i.e., 4d, 5s, and 5p for In atoms; 2s and 2p for O and C atoms; and 1s for H atoms). The calculated lattice parameter ($a_{\text{calc}} = 10.294 \text{ \AA}$) for the bixbyite structure of indium oxide, optimized using a dense Γ -centered $5 \times 5 \times 5$ k -point mesh and a higher plane-wave cutoff energy of 650 eV, agrees well with the experimental data ($a_{\text{exp}} = 10.117 \text{ \AA}$). The In₂O₃(111) surface was modeled as a periodically repeated $p(1 \times 1)$ slab consisting of five O–In–O trilayers, separated by a vacuum space of 16 Å, and was optimized using a Γ -centered $(3 \times 3 \times 1)$ k -point mesh. In each surface, the three outermost O–In–O trilayers were allowed to relax, whereas the two bottom-most layers were fixed in their bulk positions. The climbing image nudged elastic band (CI-NEB) method was employed to locate the transition states [25]. The nature of all reaction minima and transition states was confirmed by means of numerical frequency analyses. All of the relevant structures can be retrieved from the ioChem-BD database [26]. Gibbs free energies were computed using the ideal-gas approximation for gaseous species and considering only vibrational contributions for the adsorbed species. The rate coefficients for each of the elementary steps were evaluated employing the thermodynamic and kinetic parameters and the partition functions obtained from the DFT calculations and according to Transition State Theory [27]. Microkinetic simulations were performed applying a differential reactor model operated under steady-state conditions [28]. The set of equations in the microkinetic model was resolved with Maple[™]. In the simulations, temperature and partial pressures were set to the values employed experimentally and the catalyst surface was initially free of any adsorbate. From the microkinetic model, several parameters were obtained, like the apparent activation energy and the reaction orders for the reactants and products, according to the method described elsewhere [28]. Energy values were probed using (i) direct DFT results and (ii) alternative DFT results obtained in the presence of a water molecule, which was found to facilitate the first two elementary steps of the RWGS reaction, lowering

the energy of the corresponding transition states by 0.19 and 0.16 eV, respectively.

3. Results and discussion

3.1. Catalyst properties

Bulk In₂O₃ for experimental investigations was prepared by precipitation of In(OH)₃ followed by calcination in static air, as reported earlier [10]. N₂ sorption evidenced a type IV isotherm, typical of nanocrystalline materials (Fig. S2). A surface area of 123 m² g⁻¹ and a total pore volume of 0.38 cm³ g⁻¹ were calculated, which are in agreement with previous data on this catalyst. Powder X-ray diffraction (XRD) confirmed the sole presence of the cubic bixbyite structure of indium oxide (ICDD 01-088-2160, Fig. 1a) and estimation of the particle size by application of the Scherrer equation led to a value of ca. 8 nm, which is only slightly smaller than that published earlier. The profiles obtained by H₂-TPR (Fig. 1b) and CO₂-TPD (Fig. 1c) are comparable to those collected in our previous study. HRTEM (Fig. 1d) visualized crystallites of ca. 8 nm, in line with the XRD analysis, which form aggregates. Lattice fringes, visible at multiple locations, almost exclusively indicate a d spacing of 0.29 nm, corresponding to the (2 2 2) plane of In₂O₃, which is a multiple of the (1 1 1) plane. These observations are in good agreement with the energies calculated by DFT for the low Miller index terminations of In₂O₃ under vacuum (Fig. 1a, inset). The (1 1 1) surface is more stable than the (1 1 0) surface and the reconstructed oxygen-terminated (1 0 0) surface by 0.30 and 0.92 J m⁻², respectively, in line with previous computations [20]. Hence, the equilibrium Wulff construction results in an octahedral nanoparticle exposing (1 1 1) facets (Fig. 1a, inset). It should be remarked that such a model is solid, since the typical particle size is significantly larger than 3.5–4 nm, below which deviations from the equilibrium geometry might be plausible.

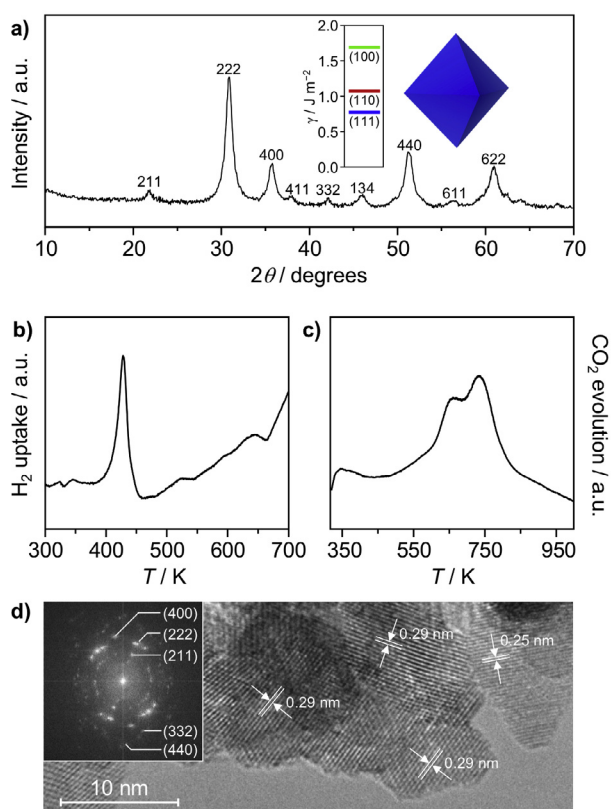


Fig. 1. (a) XRD, (b) H₂-TPR, (c) CO₂-TPD, and (d) TEM and corresponding electron diffraction pattern obtained by fast Fourier transform of bulk In₂O₃. The inset in (a) shows the Wulff construction of In₂O₃, highlighting its octahedral morphology and the exclusive exposure of (1 1 1) terminations as well as the energies calculated for low Miller-index surfaces.

Recent theoretical and experimental studies [29–31] support the formation of nanooctahedra under oxygen-rich atmospheres, such as that applied upon calcination. Although the computations by Chen et al. [30] suggest a truncated-cube as the thermodynamically more stable morphology of the oxide under CO₂ hydrogenation conditions, analysis of In₂O₃ after reaction shows negligible restructuring [10]. This hints that a transition among structures is kinetically hindered. This, along with the outstanding stability of In₂O₃ in a 1000-h test, opens the door to a reliable kinetic analysis. In addition, it justifies the unprecedented use of the (1 1 1) termination as the most representative model for the catalyst for molecular-level investigations of CO₂ hydrogenation by theoretical methods.

3.2. Kinetic analysis

The dependence of the reaction rate on the experimental parameters was investigated relating the catalytic data obtained at variable temperature and partial pressures of reactants and (by)products to the values obtained under standard conditions. These comprised a temperature of 573 K, a flow with a rate of 40 cm³_{STP} min⁻¹ composed of CO₂ and H₂ in a molar ratio of 1:4, and a GHSV of 38,000 h⁻¹, which ensured testing under a differential regime.

To estimate the apparent activation energies ($E_{a,app}$) for CO₂ hydrogenation to methanol and the RWGS reaction, catalytic tests were carried out varying the temperature between 273 and 673 K. Upon each 25 K increment of the temperature, a raise in CO₂ conversion was observed, accompanied by a drop in methanol selectivity. The suspected onset of thermodynamic equilibrium at

temperatures above 623 K was confirmed by calculations (Fig. S3). Thus, the data collected at this and higher temperatures were not considered in the linearization. From the Arrhenius plot presented in Fig. 2a, apparent activation energies of 103 kJ mol⁻¹ (1.07 eV) and 117 kJ mol⁻¹ (1.21 eV) were derived for methanol synthesis and the RWGS reaction, respectively. The higher activation energy for the competitive transformation is in line with the observed low selectivity towards CO.

The apparent reaction orders of the reactants were determined by performing measurements altering the partial pressures of CO₂ and H₂ (Fig. 2b) and normalizing the observed reaction rates (r_i) by the rate under the standard conditions (r_0) (Fig. S4a, b).

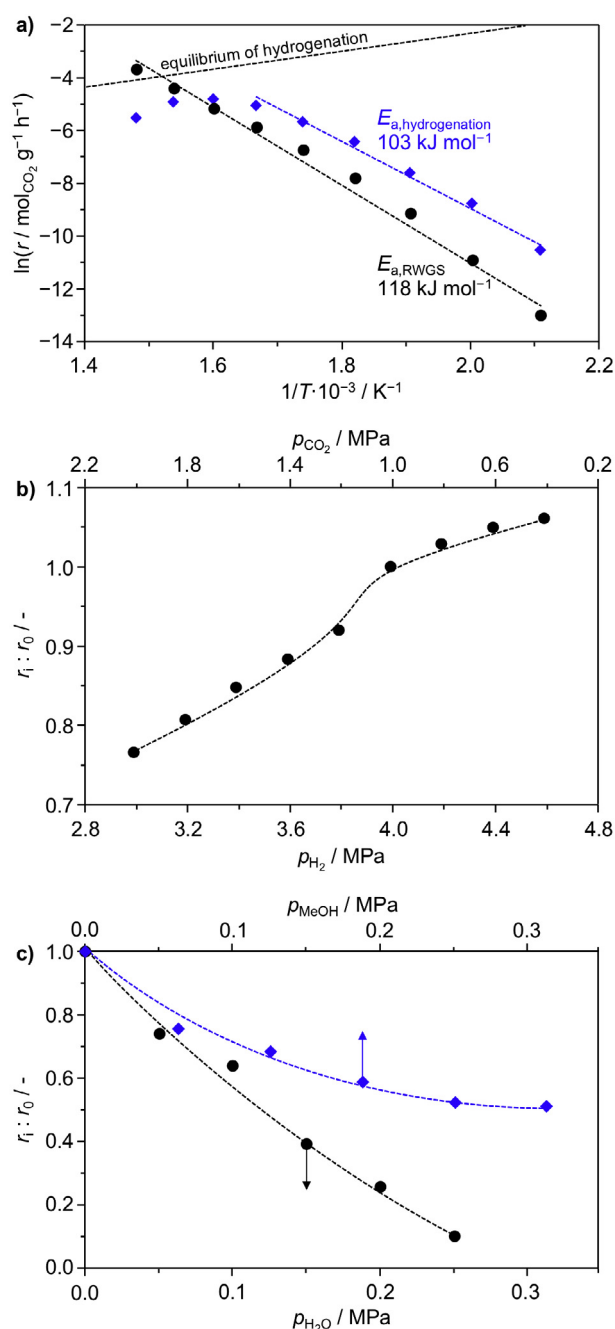


Fig. 2. (a) Arrhenius plot for CO₂ hydrogenation to methanol and the RWGS reaction over In₂O₃. Dependence of the rate on the partial pressure of (b) reactants and (c) products. Observed rates (r_i) are normalized to that at standard conditions (r_0) of $P = 5$ MPa, $T = 573$ K, and $H_2:CO_2 = 4$.

Interestingly, two sets of values were determined for both species. Above the stoichiometric ratio of $\text{CO}_2:\text{H}_2 = 1:3$, the orders were calculated at -0.1 for CO_2 and 0.5 for H_2 . Below the standard conditions, they assumed values of -0.4 and 0.8 , respectively. This variation is predominantly due to the fact that the parasitic RWGS reaction is favored in an excess of CO_2 (Fig. S5). Consequently, targeting high methanol productivity, the process should be carried out with the highest possible excess of H_2 , since this will not only enhance CO_2 conversion but also be beneficial to the selectivity towards the alcohol.

The effect of the products on the reaction kinetics was explored in a similar way to that of the reactants. Fig. 2c evidences that an increase of the methanol concentration has a minor effect on the reaction rate, while the presence of water significantly inhibits both CO_2 hydrogenation and the RWGS reaction. The apparent reaction orders with respect to the products were found to be -0.2 for methanol and -0.9 for water (Fig. S4c,d). In line with this, TPD experiments conducted at atmospheric pressure using the two species as adsorbates (Fig. 3) show that the alcohol desorbs at a much lower temperature than water (peak maxima at 492 versus 613 K). It should be mentioned that minor amounts of methylformate were formed at the higher methanol concentrations investigated. The generation of this compound, which is not observed under standard conditions, is rationalized based on the reaction between methanol and the CO byproduct, a transformation that is applied at the industrial scale to produce this chemical [32]. Remarkably, when more than 0.15 MPa of water were present in the gaseous feed significant catalyst deactivation was observed, which limited the range of partial pressures that could be probed to explore the kinetic effect of this compound (Fig. S4d). Indeed, a progressive depletion of the activity over 12 h was observed when feeding a stream containing water in a 5-times higher amount ($p_{\text{H}_2\text{O}} = 0.125$ MPa) than that generated upon CO_2 hydrogenation under standard conditions (Fig. S6). Analysis by XRD and N_2 sorption of the used sample (Fig. S7) evidenced a substantial increase of the particle size (from 8 to 18 nm) and drop in the surface area (from 123 to $47 \text{ m}^2 \text{ g}^{-1}$), which point to sintering as the main cause of deactivation. Since the presence of water in the feed is unlikely under practical conditions, its impact on the catalyst was not investigated further.

On the contrary, co-feeding of CO, the chief byproduct of this process, is highly likely and may for example be attained through a recycling stream. Earlier, it has been shown that the presence of this reducing gas can boost the catalytic activity, forming additional oxygen vacancies *in situ*, which are identified as the active sites [10]. However, by adding this compound to the feed in the absence of an inert gas, i.e., at a substantially higher partial pressure of hydrogen, a decrease in the overall activity was

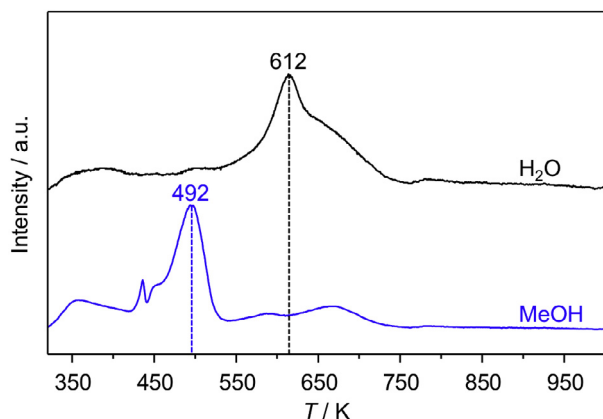


Fig. 3. H_2O - and MeOH -TPD profiles of bulk In_2O_3 .

observed. To understand the role of CO further, In_2O_3 was tested at variable total pressure ($P = 3.5, 4.5, \text{ or } 5.5$ MPa) in a stream with a molar $\text{CO}_2:\text{H}_2:\text{He}$ ratio of 1:4:0.5 adding progressively higher amounts of CO (16–70 times the quantity produced during reaction, $p_{\text{CO}} = 0.2\text{--}0.8$ MPa) and correspondingly decreasing the inert carrier content to ensure that the total flow of CO_2 and H_2 remained the same as for the other kinetic tests (Fig. 4a).

The admission of CO to the feed led to the expected increase in the methanol space-time yield (STY_{MeOH}) at the lowest pressure, to a slight drop of this parameter at the intermediate pressure, and to a significant decrease in activity at the highest pressure. This set of measurements suggests that there are partial pressures of reducing ($\text{H}_2, \text{ CO}$) and oxidizing (CO_2) agents in the feed stream for which the surface of the catalyst comprises a high abundance of vacancies but is not yet overly reduced. The role of CO as a reagent cannot be accurately assessed without the use of isotopically labelled gases. However, the experiment conducted at the lowest pressure (3.5 MPa) hints that the catalyst is somewhat active for CO hydrogenation to methanol. Indeed, the ratio of $\text{CO}_{\text{in}}:\text{CO}_{\text{out}}$ was constant at 1.1 and the mass balance was closed and no other products other than methanol were detected. The performance in pure CO hydrogenation could not be accurately assessed, as the feeding of a $\text{CO}:\text{H}_2 = 1:2$ mixture led to quick (<1 h) deactivation of In_2O_3 , as previously reported [10]. Still, the first chromatogram collected after 20 min on stream suggested a CO conversion of 2% to methanol at 573 K and 5 MPa. Clearly, it is not possible to conclude whether CO is hydrogenated to the alcohol directly or transformed into CO_2 by reaction with surface O atoms of the material, which is converted into the alcohol in a second step.

To gather further insights into the reducing effect of CO, the catalyst was exposed to gradually more elevated concentrations of this species. Specifically, In_2O_3 was firstly contacted for 5 h with a gas mixture containing CO_2 and H_2 in the same molar ratio as applied under the standard conditions and an inert gas (He) in an amount equal to that of CO_2 . Then, 0.2, 0.5, or 0.8 MPa of CO were added to the gas feed for 3 h while correspondingly decreasing the quantity of inert carrier gas. Finally, the initial conditions were restored (Fig. 4b). The admission of CO to the stream led to a decrease in activity in the range of what observed in the measurements depicted in Fig. 4a. Upon restoring the initial feed conditions, the solids exposed to the lowest and intermediate CO pressures regained their original performance, whereas the catalyst contacted with the highest amount of CO reactivated only partially. In addition, the recovery of functionality was not immediate, as in the two other experiments, but was achieved over 4 h on stream.

Samples were extracted from the reactor at different stages during the experiments just described, i.e., after 1 h on stream under standard conditions, after exposure to the stream containing an intermediate amount of CO, and after returning to the initial conditions from the feeds with intermediate and high CO concentrations (points A, B, and C in Fig. 4b, respectively), and analyzed by UV-vis and Raman spectroscopy using the fresh material as a reference (Fig. 4c,d). Since indium oxide is a semiconductor, the presence of oxygen vacancies has been indicated to lower the energy gap between valence and conduction bands [33], which can be probed by these techniques, thus gaining a qualitative indication about such defects in its structure. As-prepared In_2O_3 produced a strong band in the 240–320 nm region of the UV-vis spectrum, which overlaps with a second equally intense band between 320 and 450 nm. The first is specific to the stoichiometric oxide [34], while the second is indicative of oxygen vacancies [21]. Indeed, a smaller band gap leads to a red shift of the signal. After exposure to the reducing reaction environment (sample A), a broad absorbance in the visible range was additionally detected along with a slight increase of the intensity of the band close to the visible

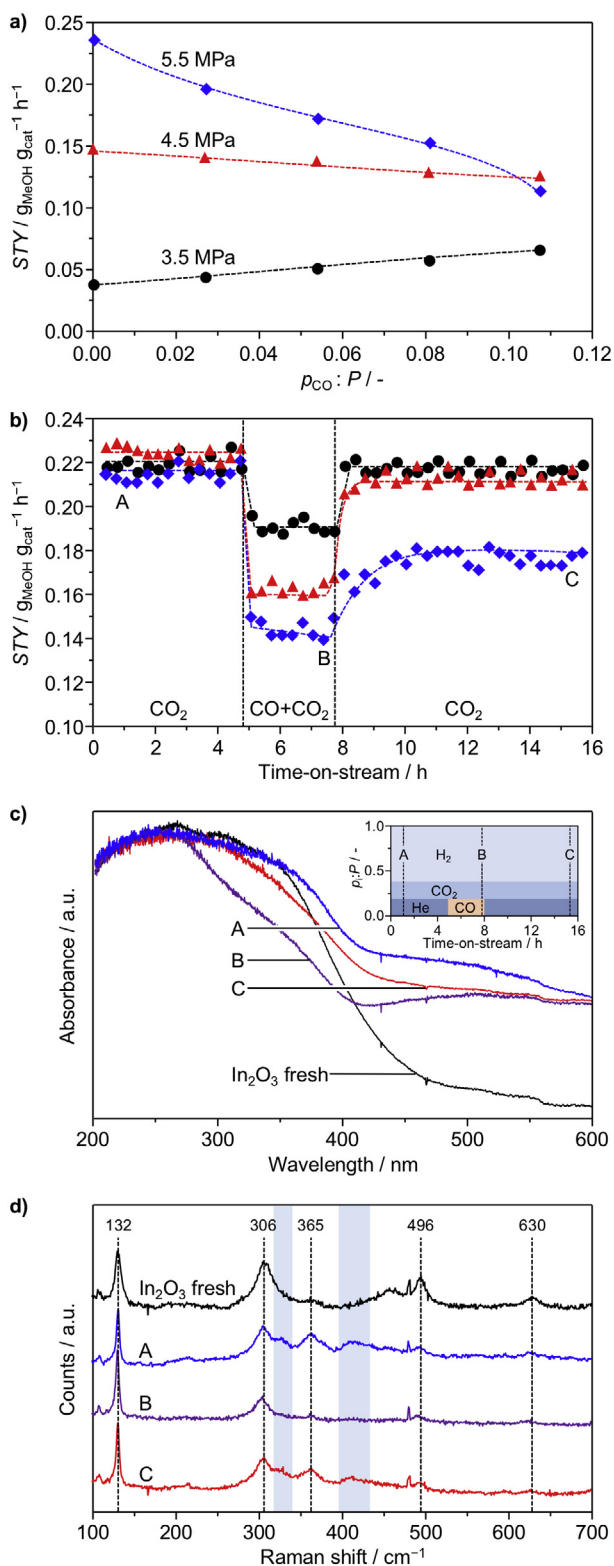


Fig. 4. (a) Evolution of the STY_{MeOH} upon replacing He in the feed by progressively higher amounts of CO (a) at different total pressures and (b) at 5.5 MPa with subsequent restoration of initial feed mixture. (c) UV-vis and (d) Raman spectra of the fresh catalyst and of samples extracted from the reactor at specific points corresponding to the labels in (b). The inset in (c) shows the relative amount of reactive and inert gases to which samples A–C were exposed. Dashed lines and blue-highlighted regions in (d) indicate the bands associated with bulk In_2O_3 and oxygen vacancies, respectively.

region, which evidence a higher concentration of oxygen vacancies, as expected. The band located at 320–450 nm became weaker after contact of the catalyst with the intermediate CO amount (sample B), likely due to the formation of islands of metallic In. The spectrum of the material exposed again to the standard feed (sample C) comprises the same features as in the spectra of samples A and B, but their intensity is midway, in line with the only partial recovery of the initial activity level. Similar trends are evident from the Raman spectra. In this case, the presence of vacancies causes the broadening of the scattering phenomena 306, 496, and 630 cm^{-1} associated with InO_6 octahedra [35]. The feature at 306 cm^{-1} is particularly sensitive to vacancies, which cause an asymmetric broadening of the Raman band towards the far infrared region accompanied by the appearance of a new signal between 400 and 430 cm^{-1} [36,37]. These features are clearly evident in samples A and C, whereas they are absent in sample B. XRD analysis (not shown) indicated no significant changes in morphology and particle size in any of the samples. Overall, these data suggest that, unless the oxide has been excessively reduced, the surface reaction $In_xO_y + CO \rightleftharpoons In_xO_{y-1} + CO_2$ is in fact a reversible process, dependent on the partial pressures of the two carbon oxides at a given H_2 concentration.

3.3. Reaction mechanism

Under relevant hydrogen pressures, a partial reduction of the $In_2O_3(111)$ surface occurs through the homolytic dissociation of molecular hydrogen forming two surface OH groups, followed by concomitant water formation and desorption and the generation of an oxygen vacancy. As recently reported [20], the conditions applied upon hydrogenation reactions favor a surface configuration, in which one oxygen vacancy per unit cell is predominantly exposed, that is also hereon considered. Indeed, the energy required to abstract a second O atom in the same lattice unit was found to be so high that this event is unlikely even under high pressures of H_2 . H_2 is activated heterolytically as $H^{\delta+}-H^{\delta-}$ at the In_3O_5 ensemble that surrounds the vacancy (Fig. 5a). While $H^{\delta+}$ binds to one oxygen atom, the species holding the negative charge

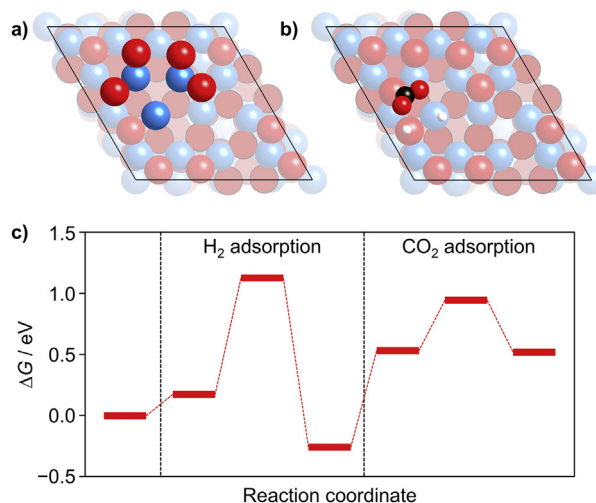


Fig. 5. (a) Top-view of the $In_2O_{3-x}(111)$ surface, with an oxygen vacancy per (1×1) cell, surrounding the outlined In_3O_5 ensemble. (b) Top view of the activated co-adsorption of CO_2 and H_2 on $In_2O_{3-x}(111)$. Color code: In (blue), O (red), C (black), and H (white). The In and O atoms in the outermost layer are represented as solid three-dimensional spheres, while those in the second and third outermost layers as two-dimensional spheres colored in a progressively lighter color. (c) Gibbs energy profile for the activation of reactants. Conditions: $P = 5$ MPa and $T = 573$ K.

is accommodated at one In atom and its electron density is delocalized among the three In atoms of the ensemble. Thus, indium oxide is capable of selectively activating hydrogen such that the polarity of the $H^{\delta+}-H^{\delta-}$ species is preserved, in a similar way to materials containing frustrated Lewis pairs [38,39]. This H_2 activation is exergonic ($\Delta G = -0.44$ eV) and associated with an activation free energy of 0.95 eV. CO_2 chemisorbs at the ensemble, adjacent to the $OH^{\delta+}$ and $InH^{\delta-}$ groups formed (Fig. 5b), surpassing an activation barrier of 0.41 eV (Fig. 5c). This configuration, i.e., a surface containing one oxygen vacancy per unit cell, chemisorbed CO_2 , and heterolytically dissociated H_2 , is the only stable starting situation for CO_2 hydrogenation. Indeed, the formation of a C–H bond from a homolytically dissociated H_2 , as it would happen over the stoichiometric surface, exhibits an activation free energy of 3.37 eV. Therefore, oxygen vacancies are required for the reaction to proceed under practical conditions. CO, when present in the feed, can increase the vacancy formation rate ($\Delta G = -0.29$ eV).

The reaction profile expressed in terms of the Gibbs free energy at 573 K and 5 MPa is depicted in Fig. 6 and the structures of all adsorbates are presented in Fig. S8. For the sake of clarity, the activation of the reactants shown in Fig. 5 is lumped in a single step in this figure. The reaction profile in terms of internal energy at 0 K is plotted in Fig. S9 for comparison. The hydride in the $InH^{\delta-}$ species formed upon H_2 activation is transferred to the chemisorbed CO_2 giving rise to a formate species, CHO_2^- (Fig. 6, red path). This process has an activation free energy of 0.44 eV and is exergonic by -1.0 eV. Then, a proton transfer forming chemisorbed formic acid takes place in a more energy-demanding step ($\Delta G^\ddagger = 1.32$ eV) characterized by a reaction free energy of 1.17 eV. The alternative transfer of the surface $H^{\delta-}$ to produce COOH and the subsequent proton transfer to form formic acid has a prohibitive activation free energy ($\Delta G^\ddagger = 1.95$ eV). Then, a second H_2 molecule is heterolytically adsorbed onto an In–O pair adjacent to the chemisorbed formic acid intermediate. Again, the $H^{\delta-}$ is inserted into the intermediate to form CH_2OOH in a step with low activation energy ($\Delta G^\ddagger = 0.29$ eV) that is exergonic by -0.81 eV. From this intermediate two scenarios arise: (i) the oxygen in CH_2OOH bound to the vacancy surface site is protonated, or (ii) its hydroxyl group is protonated, with concomitant dissociation into CH_2O and H_2O .

Following the first route (Fig. 6, maroon path), the formation of $CH_2(OH)_2$ requires 1.21 eV and results in a free energy increase of 0.97 eV. After the heterolytic adsorption of a third H_2 molecule, a hydroxyl group dissociates from the intermediate, filling the vacancy site. This step, which exhibits an activation free energy

of 0.45 eV and is exergonic by -0.09 eV, also encompasses a proton transfer to a surface oxygen leading to physisorbed formaldehyde. The latter readily reacts with the hydride to form methoxide, in view of the negligible activation energy and high exergonicity ($\Delta G = -1.30$ eV). Finally, the methoxide is protonated and methanol desorbs with an associated desorption free energy of -0.27 eV. The two surface hydroxyl groups can combine generating water, which desorbs in an overall endergonic process ($\Delta G = 0.88$ eV).

Along the second path (Fig. 6, orange path), the CH_2OOH intermediate dissociates into CH_2O and OH^- ($\Delta G^\ddagger = 0.89$ eV, $\Delta G = -0.15$ eV), the latter being subsequently protonated to form water ($\Delta G = 0.36$ eV), which desorbs ($\Delta G = -0.14$ eV). A third H_2 molecule is heterolytically dissociated at an In–O pair next to the chemisorbed formaldehyde. The $H^{\delta-}$ is transferred to CH_2O forming methoxide, a step which requires only 0.48 eV and is exergonic by -1.33 eV. The methoxide is finally protonated in a rather demanding step ($\Delta G^\ddagger = 1.37$ eV, $\Delta G = 1.07$ eV) and the resulting methanol desorbs spontaneously (-0.21 eV).

The two paths discussed above describe the consecutive addition of three heterolytically activated H_2 molecules, which implies the alternate transfer of negatively and positively polarized hydrogen atoms. The co-adsorption of multiple H_2 molecules could allow the formation of several C–H or O–H bonds consecutively. In contrast, Ye *et al.* [17] reported a mechanism on the (1 1 0) surface in which methanol is formed by three consecutive hydride additions followed by a proton transfer and each elementary step is considered independently, adding neutral hydrogen atoms, which might cause their electrons to have an exceedingly high chemical potential. Given the complexity of the In_2O_3 electronic structure, such approach might lead to artificially low barriers. Thus, the co-adsorption of multiple H_2 molecules was assessed (Fig. 6, green path).

After the initial $H^{\delta-}$ transfer leading to CHO_2 , another H_2 is adsorbed on the surface heterolytically next to the intermediate. The $H^{\delta-}$ is transferred to the intermediate to form CH_2O_2 ($\Delta G^\ddagger = 1.15$ eV, $\Delta G = 0.16$ eV). The co-adsorption of a third H_2 molecule next to the intermediate and the two hydroxyl groups is highly unfavored, as the step is endergonic by 1.10 eV. Moreover, the activation free energy of the $H^{\delta-}$ to form CH_3O^- adds up 1.19 eV, making the whole process prohibitive with a net barrier of 2.29 eV. Conversely, the formation of CH_2OOH from CH_2O_2 and a surface hydroxyl group only requires 0.69 eV. Therefore, the consecutive formation of two C–H bonds followed by an O–H bond to obtain

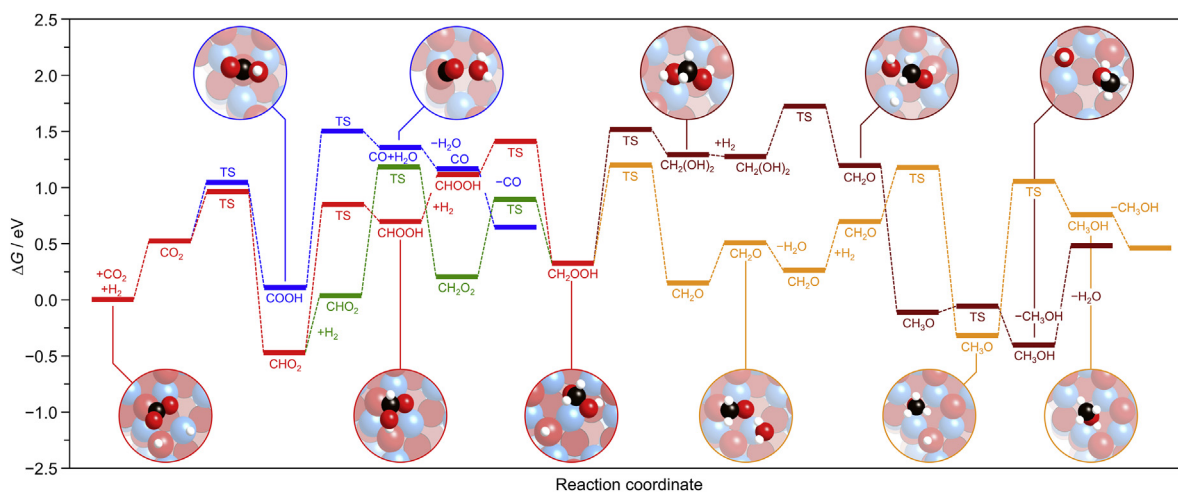


Fig. 6. Gibbs energy profile for the hydrogenation of CO_2 through the most representative paths. The hydrogenation of CO_2 to CH_2OOH is shown in red. The two possible routes to CH_2OH from this species are depicted in orange and maroon. The alternative formation of CH_2OOH from CHO_2 through the co-adsorption of two H_2 molecules is shown in green. The RWGS reaction is marked in blue. Conditions: $P = 5$ MPa and $T = 573$ K. Same color coding as in Fig. 5. TS = transition state.

CH₂OOH is favored over the alternative route, but the direct formation of CH₃O⁻ is highly unlikely. The mechanism from CH₂OOH proceeds as described above. Overall, the mechanism of CO₂ hydrogenation on In₂O₃ can be understood as a hydride-proton transfer, hence resembling transfer-hydrogenation reaction schemes. The analogous action mode of indium oxide to oxides containing frustrated Lewis pairs ensures a higher control on the reaction selectivity. Indeed, even if methanol desorption was thermodynamically less favorable, the polarity of the H species present at the surface would be insufficient to drive its further transformation into methane.

The competitive formation of CO *via* the RWGS reaction has also been evaluated in the presence of one additional water molecule (Fig. 6, blue path). Neglecting the effect of H₂O present in the environment would lead to an overestimation of the activation energies involved in the route, since this compound facilitates reaching the transition states. After the initial co-adsorption of CO₂ and H₂, the H^{δ-} can transfer to an O atom instead to the C atom giving rise to COOH rather than CHO₂ ($\Delta G^\ddagger = 0.62$ eV, i.e., 0.18 eV higher than to form CHO₂, $\Delta G = 0.42$ eV). The proton transfer to this same oxygen leading to CO and H₂O requires 1.49 eV and the process is endergonic by 1.16 eV. Finally, the desorption of the two products are exergonic steps ($\Delta G = -0.15$ and -0.39 eV, respectively). Catalyst poisoning by the COOH species, the conversion of which is most demanding along this route, is unlikely since the reverse reaction has a barrier (1.1 eV) that can be overcome under the experimental conditions.

3.4. Microkinetic modeling

Based on the DFT results, microkinetic simulations were conducted considering a differential reactor operated under the conditions experimentally applied, to assess the dependence of the reaction rate on the temperature and the partial pressures of reactants and products. Apparent activation energies of 1.73 eV (166 kJ mol⁻¹) and 1.96 eV (189 kJ mol⁻¹) were calculated for CO₂ hydrogenation to methanol and the RWGS reaction, respectively (Fig. S10a). These are higher than the corresponding values obtained from the experimental results (Fig. 2a), since the influence of the thermodynamic equilibrium is not considered in the calculations while it is never fully suppressed in the actual tests. To account for these deviations, a tangent was asymptotically fitted to the empirical data at low temperatures, as far away from the equilibrium-influenced region as permitted (Fig. S10b). In this way, the computed apparent activation energies converge to 1.56 eV (150 kJ mol⁻¹) for CO₂ hydrogenation and 1.85 eV (179 kJ mol⁻¹) for the RWGS reaction, which are in reasonable agreement with the theoretical values. These results show that even an elusive parameter such as the activation energy was qualitatively well reproduced in the simulations. Most importantly, the difference in the activation energies for the desired and competitive reaction, which controls the selectivity of the process, is 0.23 eV based on the theoretical data, which properly compares with the experimentally determined gap of 0.29 eV.

With respect to the reaction orders, that for hydrogen was positively defined (0.33), while the value determined for CO₂ is zero. The detrimental effect of water and methanol were properly retrieved with reaction orders of -0.57 and -0.14 , respectively (Fig. S11). Therefore, all the computed reaction orders are in good agreement with the experimental data, with errors within 0.15. The exception is water, for which the deviation is 0.33, a difference which is likely caused by microsolvation effects. Hence, the DFT modeling is qualitatively solid and the reason behind the discrepancy lies in second order terms, i.e., the assistance of water molecules to key selectivity-determining steps.

4. Conclusions

In this study, the mechanistic and kinetic fingerprints of CO₂ hydrogenation on In₂O₃ were elucidated in detail. The apparent activation energy experimentally determined for CO₂-based methanol synthesis was found to be higher than the one for the RWGS reaction, which explains the superior methanol selectivity of this catalyst. The methanol formation rate slightly diminished when applying higher CO₂ concentrations, in view of the moderate promotion of the RWGS reaction, while it was significantly boosted at higher H₂ contents, which enhanced both CO₂ conversion and methanol selectivity. With respect to the impact of the products concentration on the reaction rate, methanol caused a minor inhibition, whereas water was strongly detrimental. These findings were corroborated by temperature-programmed desorption experiments, showing that methanol evolves from the oxide at a 120 K lower temperature than water. It was also observed that water and the CO byproduct led to catalyst deactivation due to sintering and over-reduction when their concentrations were 4 and 20-times higher than the amounts produced by the reaction under standard reaction conditions, respectively. In the case of CO, the activity was partially depleted due to surface reduction also for quantities equal to 10–20 times of the typical amount, but could be restored upon removal of CO from the feed owing to *in situ* reoxidation by CO₂. Structural characterization of the In₂O₃ catalyst evidenced a dominant exposure of the (1 1 1) termination, which was in line with the Wulff construction calculated for this material. Theoretical modeling of CO₂ hydrogenation over this surface evidenced that the oxygen vacancies generated under the reaction conditions can activate CO₂ and heterolytically split H₂. The H^{δ+}-H^{δ-} species formed in the latter process are stabilized by the In₃O₅ ensemble surrounding the vacancy, hence preserving their polarity. Accordingly, the reaction was considered to proceed *via* the selective and consecutive addition of hydrides and protons, rather than H radicals as previously reported. Two plausible paths to methanol were outlined, which follow identical steps until the second hydride addition. From the CH₂OOH intermediate obtained, the route subsequently comprising the formation of methanediol is energetically favored. Microkinetic simulations provided values for the apparent activation energies of CO₂ hydrogenation and the RWGS reaction that are in good agreement with the measured data. They also led to orders for reactants and products in methanol synthesis that generally match the values experimentally obtained. This thorough investigation of the kinetic and molecular aspects of CO₂ hydrogenation over In₂O₃ will be highly instrumental to rationally guide further catalyst optimization and will be essential for an eventual reactor and process design.

Acknowledgements

Total Research & Technology Feluy and CTQ 2015-68770-R are thanked for financial support and BSC-RES for generous computational resources. Dr. S. Mitchell is thanked for the electron microscopy measurements and the Scientific Center for Optical and Electron Microscopy at the ETH Zurich, ScopeM, for the use of their facilities. Prof. R. Spolenak from ETH Zurich is acknowledged for access to Raman spectroscopy.

Appendix A. Supplementary material

The computed structures can be retrieved from the ioChem database at: <https://doi.org/10.19061/iochem-db-1-63>.

References

- [1] E.V. Kondratenko, G. Mul, J. Baltrusaitis, G.O. Larrazábal, J. Pérez-Ramírez, Status and perspectives of CO₂ conversion into fuels and chemicals by catalytic, photocatalytic and electrocatalytic processes, *Energy Environ. Sci.* 32 (2013) 3112–3135, <https://doi.org/10.1039/c3ee41272e>.
- [2] A. Álvarez, M. Borges, J.J. Corral-Pérez, J.G. Olcina, L. Hu, D. Cornu, R. Huang, D. Stoian, A. Urakawa, CO₂ activation over catalytic surfaces, *ChemPhysChem* 18 (2017) 3135–3141, <https://doi.org/10.1002/cphc.201700782>.
- [3] E. Fiedler, G. Grossmann, D.B. Kersebohm, G. Weiss, C. Witte (Eds.), *Methanol*, Ullmann's Encyclopedia of Industrial Chemistry, vol. 23, Wiley-VCH, Weinheim, 2012, pp. 25–48, <https://doi.org/10.1002/14356007>.
- [4] K.A. Ali, A.Z. Abdullah, A.R. Mohamed, Recent development in catalytic technologies for methanol synthesis from renewable sources: a critical review, *Renew. Sustain. Energy Rev.* 44 (2015) 508–518, <https://doi.org/10.1016/j.rser.2015.01.010>.
- [5] F. Studt, M. Behrens, E.L. Kunkes, N. Thomas, S. Zander, A. Tarasov, J. Schumann, E. Frei, J.B. Varley, F. Abild-Pedersen, J.K. Nørskov, R. Schlögl, The mechanism of CO and CO₂ hydrogenation to methanol over Cu-based catalysts, *ChemCatChem* 7 (2015) 1105–1111, <https://doi.org/10.1002/cctc.201500123>.
- [6] A. Álvarez, A. Bansode, A. Urakawa, A.V. Bavykina, T.A. Wezendonk, M. Makkee, J. Gascon, F. Kapteijn, Challenges in the greener production of formates/formic acid, methanol, and DME by heterogeneously catalyzed CO₂ hydrogenation processes, *Chem. Rev.* 117 (2017) 9804–9838, <https://doi.org/10.1021/acs.chemrev.6b00816>.
- [7] W. Wang, S. Wang, X. Ma, J. Gong, Recent advances in catalytic hydrogenation of carbon dioxide, *Chem. Soc. Rev.* 40 (2011) 3703–3727, <https://doi.org/10.1039/c1cs15008a>.
- [8] K. Chen, X. Duan, H. Fang, X. Liang, Y. Yuan, Selective hydrogenation of CO₂ to methanol catalyzed by Cu supported on rod-like La₂O₂CO₃, *Catal. Sci. Technol.* (2018), <https://doi.org/10.1039/C7CY01998J>.
- [9] S. Borman, Carbon dioxide hydrogenated to methanol on large scale, *Chem. Eng. News* 94 (2016) 7.
- [10] O. Martin, A.J. Martín, C. Mondelli, S. Mitchell, T.F. Segawa, R. Hauert, C. Drouilly, D. Curulla-Ferré, J. Pérez-Ramírez, Indium oxide as a superior catalyst for methanol synthesis by CO₂ hydrogenation, *Angew. Chem. Int. Ed.* 55 (2016) 6261–6265, <https://doi.org/10.1002/anie.201600943>.
- [11] P. Gao, S. Li, X. Bu, S. Dang, Z. Liu, H. Wang, L. Zhong, M. Qiu, C. Yang, J. Cai, W. Wie, Y. Sun, Direct conversion of CO₂ into liquid fuels with high selectivity over a bifunctional catalyst, *Nat. Chem.* 9 (2017) 1019–1024, <https://doi.org/10.1038/nchem.2794>.
- [12] J. Su, D. Wang, Y. Wang, H. Zhou, C. Liu, S. Liu, C. Wang, W. Yang, Z. Xie, M. He, Direct conversion of syngas to light olefins over Zr–In₂O₃ and SAPO–34 bifunctional catalysts: design of oxide component and construction of reaction network, *ChemCatChem* (2018), <https://doi.org/10.1002/cctc.201702054>.
- [13] N. Ruia, Z. Wang, K. Sun, J. Ye, Q. Ge, C. Liu, CO₂ hydrogenation to methanol over Pd/In₂O₃: effects of Pd and oxygen vacancy, *Appl. Catal. B* 218 (2017) 488–497, <https://doi.org/10.1016/j.apcatb.2017.06.069>.
- [14] A. García-Trenco, A. Regoutz, E.R. White, D.J. Payne, M.S.P. Shaffer, C.K. Williams, PdIn intermetallic nanoparticles for the hydrogenation of CO₂ to methanol, *Appl. Catal. B* 220 (2018) 9–18, <https://doi.org/10.1016/j.apcatb.2017.07.069>.
- [15] J. Wang, G. Li, Z. Li, C. Tang, Z. Feng, H. An, H. Liu, T. Liu, C. Li, A highly selective and stable ZnO–ZrO₂ solid solution catalyst for CO₂ hydrogenation to methanol, *Sci. Adv.* 3 (2017), <https://doi.org/10.1126/sciadv.1701290>.
- [16] J. Skrzypek, M. Lachowska, D. Serafin, Methanol synthesis from CO₂ and H₂: dependence of equilibrium conversions and exit equilibrium concentrations of components on the main process variables, *Chem. Eng. Sci.* 45 (1990) 89–96, [https://doi.org/10.1016/0009-2509\(90\)87083-5](https://doi.org/10.1016/0009-2509(90)87083-5).
- [17] J. Ye, C. Liu, D. Mei, Q. Ge, Active oxygen vacancy site for methanol synthesis from CO₂ hydrogenation on In₂O₃(110): a DFT Study, *ACS Catal.* 3 (2013) 1296–1306, <https://doi.org/10.1021/cs400132a>.
- [18] J. Ye, C. Liu, Q. Ge, DFT study of CO₂ adsorption and hydrogenation on the In₂O₃ surface, *J. Phys. Chem. C* 116 (2012) 7817–7825, <https://doi.org/10.1021/jp3004773>.
- [19] M. Dou, M. Zhang, Y. Chen, Y. Yu, DFT study of In₂O₃-catalyzed methanol synthesis from CO₂ and CO hydrogenation on the defective site, *New J. Chem.* (2018), <https://doi.org/10.1039/c7nj04273f>.
- [20] D. Albani, M. Capdevila-Cortada, G. Vilé, S. Mitchell, O. Martin, N. López, J. Pérez-Ramírez, Semihydrogenation of acetylene on indium oxide: proposed single-ensemble catalysis, *Angew. Chem. Int. Ed.* 56 (2017) 10755–10760, <https://doi.org/10.1002/anie.201704999>.
- [21] G. Kresse, J. Furthmüller, Efficiency of *ab initio* total energy calculations for metals and semiconductors using a plane-wave basis set, *Comput. Mater. Sci.* 6 (1996) 15–50, [https://doi.org/10.1016/0927-0256\(96\)00008-0](https://doi.org/10.1016/0927-0256(96)00008-0).
- [22] G. Kresse, J. Hafner, *Ab initio* molecular dynamics for liquid metals, *Phys. Rev. B* 47 (1993) 558–561, <https://doi.org/10.1103/PhysRevB.47.558>.
- [23] J.P. Perdew, K. Burke, M. Ernzerhof, Generalized gradient approximation made simple, *Phys. Rev. Lett.* 77 (1996) 3865–3868, <https://doi.org/10.1103/PhysRevLett.77.3865>.
- [24] P.E. Blöchl, Projector augmented-wave method, *Phys. Rev. B* 50 (1994) 17953–17979, <https://doi.org/10.1103/PhysRevB.50.17953>.
- [25] G. Henkelman, B.P. Uberuaga, H. Jónsson, A climbing image nudged elastic band method for finding saddle points and minimum energy paths, *J. Chem. Phys.* 113 (2000) 9901–9904, <https://doi.org/10.1063/1.1329672>.
- [26] M. Álvarez-Moreno, C. De Graaf, N. Lopez, F. Maseras, J.M. Poblet, C. Bo, Managing the computational chemistry big data problem: the ioChem-BD Platform, *J. Chem. Inf. Mod.* 55 (2014) 95–103, <https://doi.org/10.1021/ci500593j>.
- [27] I. Chorkendorff, J.W. Niemantsverdriet, *Reaction Rate Theory, Concepts of Modern Catalysis And Kinetics*, vol. 1, Wiley-VCH, Weinheim, 2003, pp. 108–115, <https://doi.org/10.1002/3527602658>.
- [28] Q. Li, R. García-Muelas, N. López, Microkinetics of alcohol reforming for H₂ production from a FAIR density functional theory database, *Nat. Commun.* 9 (2018) 526–533, <https://doi.org/10.1038/s41467-018-02884-y>.
- [29] O. Bierwagen, J. Rombach, J.S. Speck, Faceting control by the stoichiometry influence on the surface free energy of low-index bcc-In₂O₃ surfaces, *J. Phys.: Condens. Matter* 28 (2016) 224006–2240013, <https://doi.org/10.1088/0953-8984/28/22/224006>.
- [30] M. Zhang, W. Wang, Y. Chen, Insight of DFT and *ab initio* atomistic thermodynamics on the surface stability and morphology of In₂O₃, *Appl. Surf. Sci.* 434 (2018) 1344–1352, <https://doi.org/10.1016/j.apsusc.2017.11.258>.
- [31] O. Bierwagen, M.E. White, M.Y. Tsai, J.S. Speck, Plasma-assisted molecular beam epitaxy of high quality In₂O₃(001) thin films on Y-stabilized ZrO₂(001) using In as an auto surfactant, *Appl. Phys. Lett.* 95 (2009) 262105–262107, <https://doi.org/10.1063/1.3276910>.
- [32] P. Zehner, K. Bittins, W. Haarde, U. Eiden, D. Wolff, M. Herr, L. Hupfer, Preparation of methyl formate, US Patent 5 401 873 (1995), to BASF AG.
- [33] F. Lei, Y. Sun, K. Liu, S. Gao, L. Liang, B. Pan, Y. Xie, Oxygen vacancies confined in ultrathin indium oxide porous sheets for promoted visible-light water splitting, *J. Am. Chem. Soc.* 136 (2014) 6826–6829, <https://doi.org/10.1021/ja501866r>.
- [34] F. Jiang, H. Zhao, H. Chen, C. Xu, J. Chen, Enhancement of photocatalytic decomposition of perfluorooctanoic acid on CeO₂/In₂O₃, *RSC Adv.* 6 (2016) 72015–72021, <https://doi.org/10.1039/c6ra09856h>.
- [35] M. Kaur, N. Jain, K. Sharma, S. Bhattacharya, M. Roy, A.K. Tyagi, S.K. Gupta, J.V. Yakhmi, Room-temperature H₂S gas sensing at ppb level by single crystal In₂O₃ whiskers, *Sens. Actuat. B Chem* 133 (2008) 456–461, <https://doi.org/10.1016/j.snb.2008.03.003>.
- [36] M. Kumar, V.N. Singh, F. Singh, K.V. Lakshmi, B.R. Mehta, J.P. Singh, On the origin of photoluminescence in indium oxide octahedron structures, *Appl. Phys. Lett.* 92 (2008) 171907–171909, <https://doi.org/10.1063/1.2910501>.
- [37] T. Bielz, H. Lorenz, W. Jochum, R. Kaindl, F. Klauser, B. Klötzer, S. Penner, Hydrogen on In₂O₃: reducibility, bonding, defect formation, and reactivity, *J. Phys. Chem. C* 114 (2010) 9022–9029, <https://doi.org/10.1021/jp1017423>.
- [38] M. Ghossoub, S. Yadav, K.K. Ghuman, G.A. Ozin, V.C. Singh, Metadynamics-biased *ab Initio* molecular dynamics study of heterogeneous CO₂ reduction via surface frustrated lewis pairs, *ACS Catal.* 6 (2016) 7109–7117, <https://doi.org/10.1021/acscatal.6b01545>.
- [39] S. Zhang, Z. Huang, Y. Ma, W. Gao, J. Li, F. Cao, L. Li, C. Chang, Y. Qu, Solid frustrated-Lewis-pair catalysts constructed by regulations on surface defects of porous nanorods of CeO₂, *Nat. Commun.* 8 (2017) 15266–15276, <https://doi.org/10.1038/ncomms15266>.